ON THE POTENTIAL OF NUCLEAR MAGNETIC RESONANCE FOR ASSESSING WATER CONTENT AND SATURATION IN MINE TAILINGS

Jorge Macedo, M.ASCE, Paola Torres, Carlos Santamarina, M.ASCE

Abstract

Nuclear magnetic resonance (NMR) exploits the interaction between atomic nuclei and an external magnetic field. Recent advancements in small-diameter probes have expanded NMR applications for shallow subsurface investigations (<100 m); however, existing efforts in tailings engineering remain scarce. This study evaluates NMR's potential to characterize water content and saturation in mine tailings. Tailings with varying particle size distributions and mineralogies, along with Ottawa sand and kaolinite, were analyzed using two NMR systems with different signal-to-noise ratios and magnetic fields. The study examines the influence of magnetic susceptibility, mineralogy, gradation, echo time, signal-to-noise ratio, and tailings pond water on NMR measurements. NMR-derived water content and saturation estimates were compared against controlled target volumetric and gravimetric measurements. Results indicate that magnetic susceptibility is a key limiting factor: NMR performed well for paramagnetic tailings with low magnetic susceptibility (<1.0 E^{-3}) but poorly for ferromagnetic tailings with high magnetic susceptibility (>1.9E^{-2}). However, low magnetic susceptibility alone does not guarantee reliable performance, as mineralogy and the presence of elements such as iron (Fe) also play a role. Additionally, the results show that shorter echo times and higher signal-to-noise ratios are beneficial. While gradation and tailings pond water primarily influenced NMR decay curves, they had minimal impact on water content estimates for the examined paramagnetic tailings. Finally, the study conducts error propagation evaluations to assess the degree of confidence in estimating volumetric water content and degree of saturation for different scenarios in tailings engineering.

Keywords: Nuclear Magnetic Resonance, volumetric water content, saturation, mine tailings.

1 Introduction

Nuclear Magnetic Resonance, NMR, relies on the interaction of atomic nuclei with nonzero spin - naturally behaving like tiny magnets with an external magnetic field (Bloch, 1946; Purcell et al., 1946). During an NMR measurement, the magnetic moments of specific nuclei, such as hydrogen protons (H^+), align with the imposed magnetic field. Once aligned, a transverse radiofrequency pulse forces the nuclei to rotate 90º, then relax back to their original orientation. The measured longitudinal and transverse fields facilitate the assessment of material characteristics such as volumetric water content (e.g., Behroozmand et al., 2015), pore size distribution (e.g., Falzone & Keating, 2016a; Jaeger et al., 2009; Keating & Falzone, 2013), and saturation (e.g., Costabel & Yaramanci, 2011; Falzone & Keating, 2016).

NMR has been extensively applied in the petroleum industry (Behroozmand et al., 2015; Chen & Li, 2019; Coates et al., 1999; Dunn et al., 2002) with large diameter probes, i.e., > 5" used for in-situ measurements. More recent small-diameter probes are suitable for shallow subsurface explorations, i.e., first 100 m (e.g., Perlo et al., 2013; D. Walsh et al., 2013), promoting applications in hydrology (e.g., Behroozmand et al., 2017; Dlubac et al., 2013; Kendrick et al., 2021; Kirkland & Codd, 2018; Knight et al., 2016; Pehme et al., 2022; Walsh et al., 2013, 2014), environmental engineering (e.g., Conte et al., 2024; Kirkland et al., 2017; Spurlin et al., 2019), and water resources (e.g., Alves Filho et al., 2015; Anaraki et al., 2021). Most previous efforts that have evaluated the NMR potential to assess water content and saturation have been focused on natural sediments, rocks, and soils (e.g., Falzone & Keating, 2016b, 2016a; Jaeger et al., 2009; Novotny et al., 2023; Sucre et al., 2011; Zhao & Santamarina, 2022). Applications focused on assessing water content and saturation of mine tailings are limited to a single technical breakthrough abstract by Reid et al. (2023) based on one tailings material only and with limited details. Other related applications include the use of NMR to monitor the hydration rate of cemented paste backfill (Nasharuddin, 2023), the settling behavior of oil sands (Motta et al., 2008), the bitumen and

48 solid contents in oils sands (Motta Cabrera et al., 2010), and the mobile water content for a tailings
49 storage facility (TSF) in New Mexico (Spurlin et al., 2019).

50 The main objective of this study is to assess the potential of NMR to characterize mine tailings,
51 focusing on the assessment of water content and saturation, which are important inputs in the design and
52 condition assessment of TSFs. The study involves mine tailings from several TSFs of varying particle size
53 distribution and mineralogies. We used two NMR systems with different signal-to-noise ratios and
54 magnetic fields to study the effects of magnetic susceptibility, gradation, mineralogy, echo time, signal-
55 to-noise ratio, and tailings pond water. Analyses explore error propagation and the degree of confidence
56 for measuring volumetric water content and saturation. To our knowledge, this study constitutes the first
57 effort to holistically assess the potential of NMR for estimating water content and saturation in mine
58 tailings. The following section introduces fundamental principles of NMR relevant to discussions in later
59 sections. Then, we describe the NMR devices utilized, the experimental procedures, the characteristics of
60 the tested tailings, and the measurement results. The analyses and discussions focus on the performance
61 of NMR in estimating volumetric water content and saturation and how measurement errors in volumetric
62 water content influence saturation estimates.

63 **2 NMR Principles**

64 Hydrogen protons, H+, have an intrinsic magnetic moment associated with their spin angular
65 momentum in a random state (Figure 1a). Protons H^+ align with an applied static magnetic field B_0 and
66 precess at the Lamor frequency $f_0 = {\gamma|B_0|}/{2\pi}$, where $|B_0|$ is the magnetic field strength, and γ is the
67 gyromagnetic ratio for H^+, γ= 2.675x10^8 rad/(s.T) (Levitt, 2008). The alignment of the protons creates a net
68 longitudinal magnetization M_z in the direction of B_0 (Figure 1b). While maintaining the longitudinal
69 magnetic field B_0, a transverse oscillating magnetic field B_1 is applied using a radio frequency RF pulse
70 with a tuned frequency f_0. This pulse rotates the proton spins into alignment with the transverse plane,
71 creating a transverse magnetization M_{xy} (Figure 1c). Once the RF is turned off (Figure 1d), the protons

relax, gradually return to their initial z-orientation, and the magnetic polarization M_z recovers asymptotically following an exponential curve, as schematically shown in Figure 1b, for a maximum M_{z0} and a time constant T_1, known as the longitudinal relaxation time. On the other hand, the transverse magnetization decays exponentially from a maximum value of M_{0xy} to zero with a time constant T_{2i}, known as the transverse relaxation time (Figure 1d).

Water relaxation in porous media is primarily caused by spinning protons colliding with the mineral surfaces. Then, the relaxation time depends on pore size, and multiple relaxation rates coexist in porous media, as schematically illustrated by Figure 1e. The recorded NMR signal combines the exponential decaying response from all pores (Figure 1e). Then, the recorded signal is a sum of decaying curves, each with its amplitude A_i and relaxation time T_{2i}. The plot of the A_i factors versus the corresponding T_{2i}times is known as the T_2 distribution. The sum of amplitudes $\sum A_i$ is proportional to water content, whereas the T_2 distribution is a proxy for the pore size distribution (e.g., Behroozmand et al., 2015; Coates et al., 1999; Dunn et al., 2002; Falzone & Keating, 2016a; Jaeger et al., 2009; Keating & Falzone, 2013).

3 NMR Devices Considered in This Study

This study used two NMR devices, Dart and Helios, from Vista Clara Inc. Table 1 lists relevant features, and Figure 2 shows their operational principles. The Helios uses a Halbach array of permanent magnets (Keating et al., 2020), and the transverse RF signal has a frequency of 454 kHz with a minimum echo spacing of 0.2 ms. The specimen to be tested is placed inside the static magnetic field B_0 (Figure 2– left column); the field is quite uniform across the measurement zone, and the gradient is very small (~0.004 T/m). The Dart probe involves a permanent magnet to create a static magnetic field $B_{0(r)}$ on the soil surrounding the probe; the gradient decreases with the radial distance, r (Figure 2– right column). A coil generates the oscillating transverse magnetic field B_1 at RF frequencies of 425 kHz and 475 kHz. Each RF frequency assesses water relaxation at two different measurement radial distances, r_1 and r_2. In both cases, the measured region, or sensitive volume, is a relatively thin shell, as illustrated in Figure 2. The

$B_{0(r)}$ gradient reaches a value of 0.1 T/m between r_1 and r_2 (significantly higher than that in the Helios device). Table 1 lists salient characteristics for the two devices, including the radial distances for the measured shells using the Dart device.

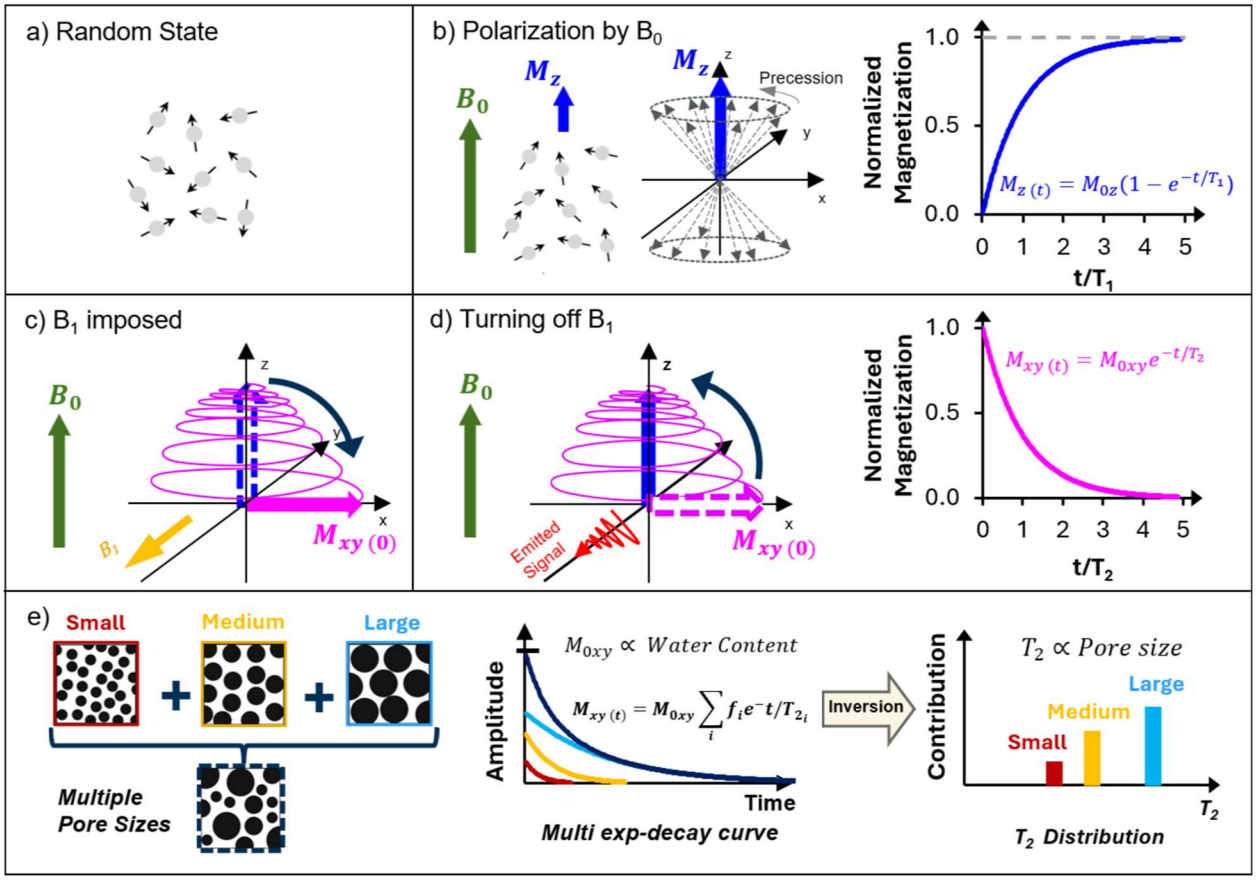

Figure 1. NMR principles. (a) Random state of H+ protons. (b) Equilibrium state after applying a static magnetic field B_0 and longitudinal magnetization. (c) Application of an oscillating magnetic field B_1. (d) Response after turning off B_1 and transverse magnetization decay. (e) Multi-exponential decaying curve illustrating the contribution from different pore sizes, the inversion process, and resulting T_2 distributions. Variables defined in the text. Figures modified after Zhao &Santamarina (2022) and Fu et al. (2021).

Table 1. Key features of the NMR devices used in this study

NMR device	Diameter/ Length	Frequency (kHz)	Sensitive shell diameters (cm)	Minimum t_e (ms)	Magnetic field gradient (T/m)
Dart	3.8cm / 172 cm	475 / 425	12 / 15	0.5**	0.1
Helios	10.2 cm / 60 cm*	454	-	0.2	0.004

* Chamber dimensions where a specimen can be placed.

** The Dart probe can be factory-calibrated to lower echo times (e.g., 0.4 ms) but at a lower signal-to-noise ratio.

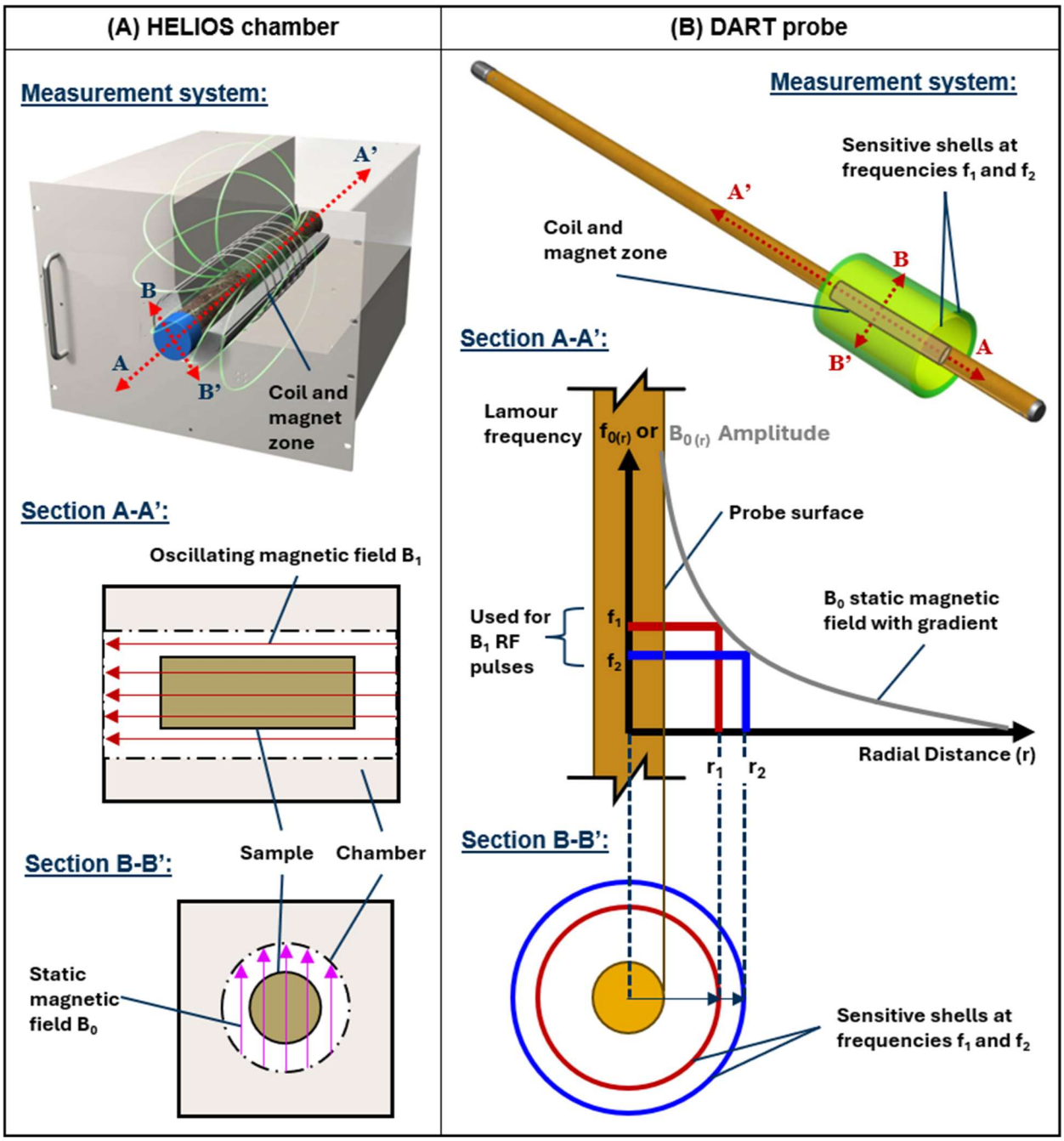

Figure 2. NMR devices used in this study. (A) Helios chamber for laboratory characterization – the specimen is housed inside the device (B). Dart insertion probe for laboratory characterization and field deployment – the sediment rests outside the probe. Modified from Coates et al. (1999) and Vista Clara Inc.

Both NMR devices use the Carr, Purcell, Meiboom, Gill (CPMG) pulse sequence to enhance the relaxation signal. (Carr & Purcell, 1954; Meiboom & Gill, 1958). The CPMG pulse refocuses the H^+ spins by applying 180° pulses tuned at the Lamour frequency after imposing an initial 90° radio frequency pulse. Refocusing is needed as the relaxation of H^+ protons can be affected by magnetic field inhomogeneities, which cause the H^+ spins to precess at slightly different Lamour frequencies. The echo time, t_e, separates the 180° pulses. The "spin echoes" between the 180° pulses created by the CPMG sequence are used to obtain the overall multi-exponential decay curve (Figure 3). The application of N pulses, resulting in a total measurement time of $N \cdot t_e$, often known as the scan length. Dunn et al. (2002) provide additional details for interested readers on CPMG pulses and their use in NMR measurements.

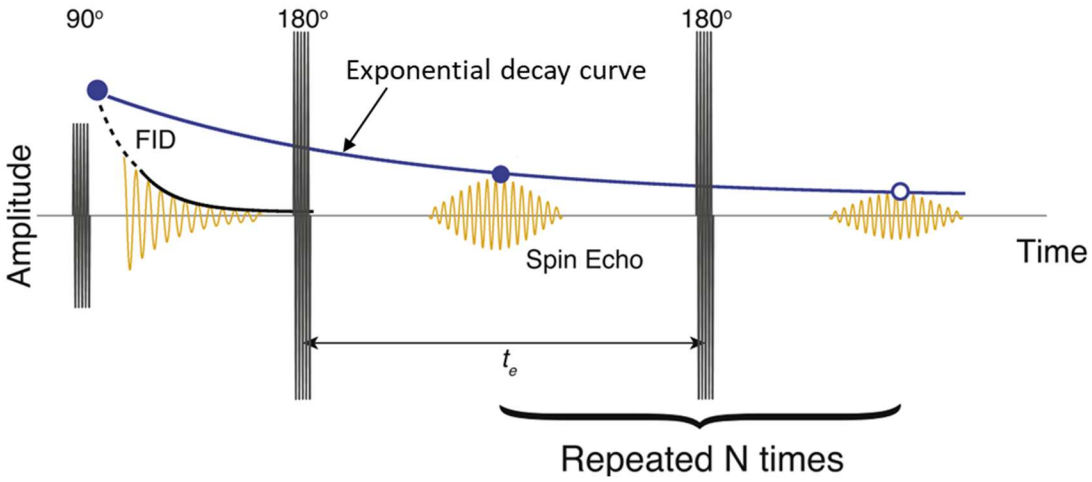

Figure 3. The CPMG pulse sequence for NMR measurements. The measurement begins with a 90° pulse, which generates a single free induction decay (FID) curve, followed by a train of N 180° refocusing pulses separated by the echo time, t_e. The spin echoes appear between refocusing pulses. The exponential decay curve is formed using the peaks of each spin echo.

The devices utilize both main and burst CPMG pulse sequences for data acquisition, a configuration commonly employed in NMR logging applications (Coates et al., 1999). The main CPMG sequence utilizes a long recovery time and scan length to allow hydrogen nuclei to become fully polarized; hence, the main CPMG collects fully polarized echo trains. In contrast, the burst CPMG sequence employs a short recovery time, resulting in the collection of partially polarized echo trains. The main and burst CPMG sequences

133 can be repeated multiple times and averaged to enhance the signal-to-noise ratio (SNR). In particular, the
134 short duration of the burst sequence allows for frequent repetition, which significantly enhances the
135 signal-to-noise ratio for rapidly relaxing signals associated with small pores.

136 **4 Materials and Experimental Procedures**

137 The experimental program involved eight mine tailings and two natural soils: Ottawa sand and
138 kaolinite. Figure 4 shows the particle size distributions of the tested mine tailings and natural soils, andlists
139 salient properties. The tailings range from silty sands to sandy silts, with fine contents FC=27 to 74%
140 (particles <#200 mesh), plasticity index PI=0 to 4, and specific surface 5.5 to 19.6 m^2/g. The specific surface
141 was measured using the methylene blue adsorption method following the European standard (spot test,
142 Santamarina et al. 2002). Consequently, these tailings are mostly non-plastic, and their specific surface
143 values suggest the absence of active clay minerals. X-ray diffraction measurements point to the main
144 mineral constituents (Table 2).

145 The material response to an external magnetic field defines its magnetic susceptibility and may
146 affect NMR measurements (Keating et al., 2020; Keating & Knight, 2007, 2008). The magnetic
147 susceptibility, χ, was measured for all materials using a vibrating sample magnetometer (Ling et al. 2022).
148 The measurements consist of vibrating a sample at a known frequency (10 to 60 Hz) and amplitude (2
149 mm) in an external uniform magnetic field, H, ranging from 0 to 40 mT. As the sample vibrates, the
150 changing magnetic flux induces an electric signal in pick-up coils, which is proportional to the magnetic
151 moment of the sample (M). This signal is then used to determine χ by analyzing how the magnetic
152 moment changes with the applied field. Specifically, χ is estimated as the slope of the *M* - *H* curve in the
153 linear region, i.e., $\chi = M/H$. Table 2 shows the measured χ values for the tested materials.

154 Inductively Coupled Plasma - Optical Emission Spectroscopy (ICP-OES Fassel & Kniseley, 1974) was
155 used to quantify the iron (Fe) concentrations in the tested tailings, as Fe influences magnetic properties.

This technique ionizes a sample using a high-temperature argon plasma, then separates and detects ions based on their mass-to-charge ratio. Table 2 shows the measured Fe concentrations.

The specimens for Helios measurements were prepared at volumetric water contents between VWC=17 and 50% and a degree of saturation between Sr=37 and 100%. We used polyethylene terephthalate glycol containers (5.2 cm in diameter and 15.3 cm in height) to avoid interference with NMR signals, as confirmed by collecting signals from a sealed empty container. Specimens with low to moderate water saturation were prepared using moist tamping, while near-saturation samples were prepared using a vacuum chamber. The unsaturated specimens were prepared by mixing pre-defined amounts of dry soil and water to satisfy target gravimetric water contents; the mixture was then tamped in seven layers to achieve pre-defined volumetric water content ranges. For the saturated specimens, the recipient was first filled with dry soil between filter papers placed at the bottom and top. The recipient was then submerged in a larger container filled with water to allow bottom-up water invasion. The recipient and the water-filled container were placed inside a vacuum chamber to facilitate specimen saturation. The mass of dry soil, water, and sample volume were recorded in all specimens, enabling the calculation of volumetric water content and saturation. Finally, the samples were introduced into the Helios chamber to gather NMR measurements.

Dart measurements were conducted inside a Faraday cage (Figure 5a) to reduce external electromagnetic noise. The setup for Dart measurements (Figure 5b, 5c) consisted of two concentric polyvinyl chloride cylinders, where the Dart probe is situated inside the inner tube, and the material to be tested is placed between the inner and outer diameters. The specimen dimensions were selected to prevent longitudinal and radial boundary effects; in particular, the sensitive shell diameters of the Dart probe listed in Table 1 fall within the annular soil specimen. The external cylinder has a 200 mm diameter and a 350 mm height. Low- to moderate-saturation specimens were prepared by mixing pre-defined amounts of dry soil and water to achieve target gravimetric water contents. The mix was then compacted

in seven layers using an annular hammer dropped from a constant height of 45 cm. The number of blows per layer and the number of layers were based on the compaction energy from the standard Proctor test. After NMR measurements, the specimen was removed from the annular container, and three small samples were taken from the center zone to confirm the gravimetric water content. High saturation specimens were prepared by water sedimentation; the annular-shaped container was filled with alternating layers of water and dry soil, with the soil being poured uniformly. The total mass of dry tailings and water added was recorded, along with the final specimen height. Final gravimetric and volumetric measurements were used to determine volumetric water content and degree of saturation for each specimen.

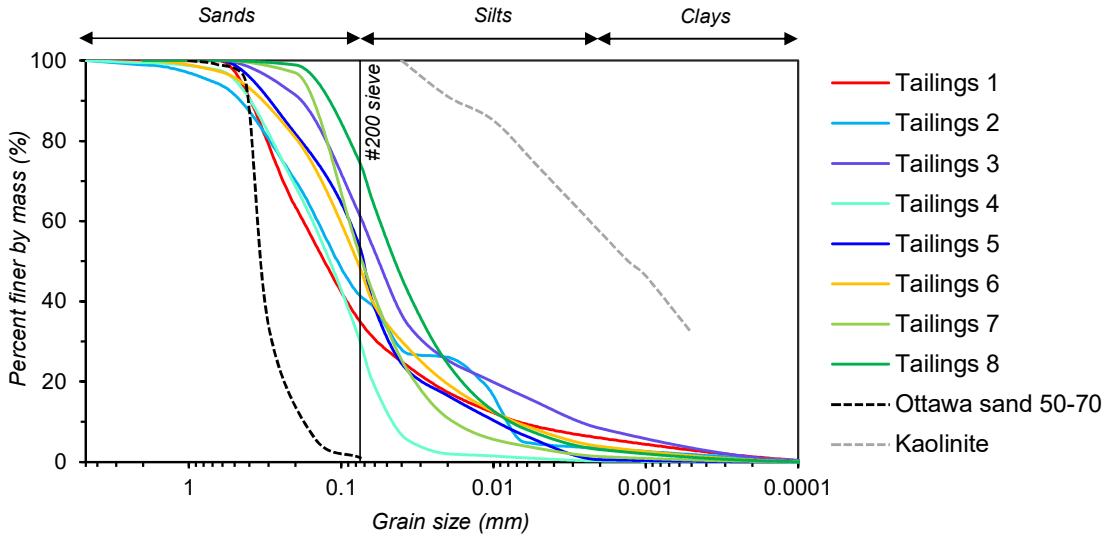

Figure 4. Particle size distribution of the tested tailings and natural soils

192 *Table 2. Properties for the tested mine tailings and natural soils*

Material	Ore source	FC/PI	SS (m2/g)	χ (SI)	Mineralogy	Fe content (%)
Tailings 1	Copper and Silver	27/0	9.2	2.80×10^{-4} (Paramagnetic)	Quartz 44.2%, Pyrite 3.9%, Microcline 33.7%, Muscovite 21.6%, Ankerite 7.2%	4.2%
Tailings 2	Polymetallic	39/0	15.9	3.41×10^{-4} (Paramagnetic)	Quartz 44.2%, Sanidine (Fe^{+3} bearing) 31.3%, Muscovite 9.0% Bassanite 6.8%, Clinochlore 3.9% Hydrononium jarosite 2.68%, Sodium mica 2.1%	4.1%
Tailings 3	Copper	70/0	7.3	1.54×10^{-1} (Ferromagnetic)	Plagioclase 39.4%, Microcline 27.6%, Clinochlore 14.8%, Ferro-actinolite 7.0%, Cronstedtite-1T 6.0%, Magnetite 2.0%, Magnesioferrite 1.8%	48.9%
Tailings 4	Molybdenum	29/0	5.5	3.34×10^{-4} (Paramagnetic)	Quartz 70.6%, Muscovite 14.3%, Orthoclase 13.6%, Wurtzite-2H 0.9%, Fluorite 0.64%	1.8%
Tailings 5	Copper	52/10	19.6	9.92×10^{-4} (Paramagnetic)	Quartz 51.2%, Sanidine (Fe+3 bearing) 21.2%, Muscovite-2M1 6.7%, Wulfenite 1.34%, Albite 1.6%, Dickite 0.82%, Rutile 17.1%	0.4%
Tailings 6	Polymetallic	56/4	10.4	1.91×10^{-2} (Ferromagnetic)	Quartz 19.2%, Pyrite 11.9%, Goethite 18.0%, Clinochlore 21.4%, Pigeonite 13.4%, Jarosite 4.9%, Phlogopite 2.6%, Scapolite 7.8%, Alumosilicate 0.9%	7.3%
Tailings 7	Molybdenum	49/0	5.5	3.72×10^{-4} (Paramagnetic)	Quartz 70.6%, Orthoclase 13.6%, Muscovite-2M1 14.3%, Wurtzite 0.9%, Fluorite 0.6%	0.9%
Tailings 8	Molybdenum	70/0	8.6	9.77×10^{-4} (Paramagnetic)	Quartz 54.10 %, Fluorite 0.7%, Orthoclase 20.4%, Muscovite 24.9%	0.8%
Ottawa Sand	-	-	-	-1.25×10^{-6} (Diamagnetic)	-	-
Kaolinite	-	-	-	7.50×10^{-6} (Non - paramagnetic)	-	-

193

(a)  (b) 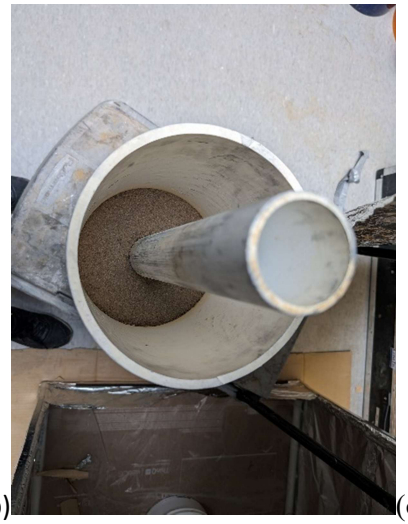 (c) 

(d) 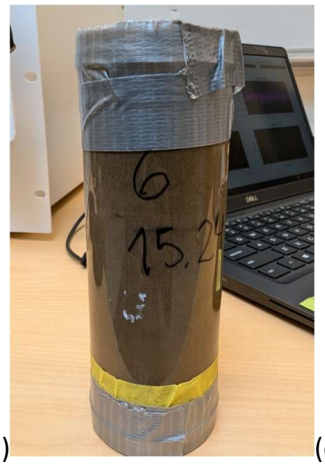 (e) 

Figure 5. (a) Fadaray Cage enabled for NMR Dart measurements, (b) top view of the PVC container with mine tailings being placed, (c) example of the Dart probe inside de Faraday cage during an NMR measurement, (d) container used for Helios measurements, and (e) set up during NMR measurements in the Helios chamber.

5 NMR Measurements and Typical Results

The parameters selected for the CPMG pulse sequences used with the Helios and Dart NMR devices are shown in Tables 3 and 4, which also summarize the number of stacks (Navg) to increase the signal-to-noise ratio, the scan length, and the recovery time TR. Selected echo time values for the Helios system were t_e =0.2, 0.5, 1.0, and 2.0 ms; the shortest echo time available with a standard calibration, t_e =0.5, was used for the Dart system.

5.1 Data reduction

T2 distributions are obtained from an inversion process. However, the volumetric water content VWC is directly related to the amplitude of the measured NMR exponential decay curve, i.e., the intercept at the origin $t = 0$ (Figure 1e). Recall that the measured NMR signal is the sum of multiple exponential decaying curves.

$$A(t) = \sum_{i=1}^{n} A_i e^{-\frac{t}{T_{2i}}} \quad (1)$$

The Taylor expansion for $t \to 0$ shows that the summation can be approximated as a single exponential function for short t values, i.e., $t \ll T_{2peak}$, where T_{2peak} corresponds to the exponential term with the largest A_i (see Appendix A for details). Then, the measured signal becomes a straight line in log(amplitude) versus time, which facilitates evaluating the signal amplitude at $t = 0$, i.e., its intercept with the y-axis, through a simple linear regression. We used this direct method to obtain the VWC; we then computed saturation using VWC from NMR and the gravimetric water content GWC measured during experiments:

$$Sr = \frac{VWC}{1 - \frac{VWC}{GWC \cdot Gs}} \quad (2)$$

where G_s is the specific gravity.

Figure 6 illustrates this data reduction procedure using a measurement with Ottawa sand. Figures 6a and 6b show multi-exponential decaying curves from Helios and Dart measurements, while Figures 6c and 6d show the measured signals in a log-linear scale. In general, the time window for the linear fitting is material-specific, and it is selected using two criteria: (1) the upper limit is below T_{2peak}, which generally exceeds 10 ms for the tested tailings, and (2) at least 10 data points from the initial portion of the decay curves are included in the fitting.

For the Ottawa sand example, the estimated VWCs are 28.9% (Helios) and 29.3% (Dart), closely matching the target values of 28.9 % (Helios) and 31.5 % (Dart). The estimated saturation values are 69.1% (Helios) and 71.9% (Dart), also closely aligned with the targets of 69.1% (Helios) and 72.7% (Dart). The described

procedure is consistently applied in evaluating the collected data. The following sections present typical results for the different tailings and discuss key factors that influence NMR measurements.

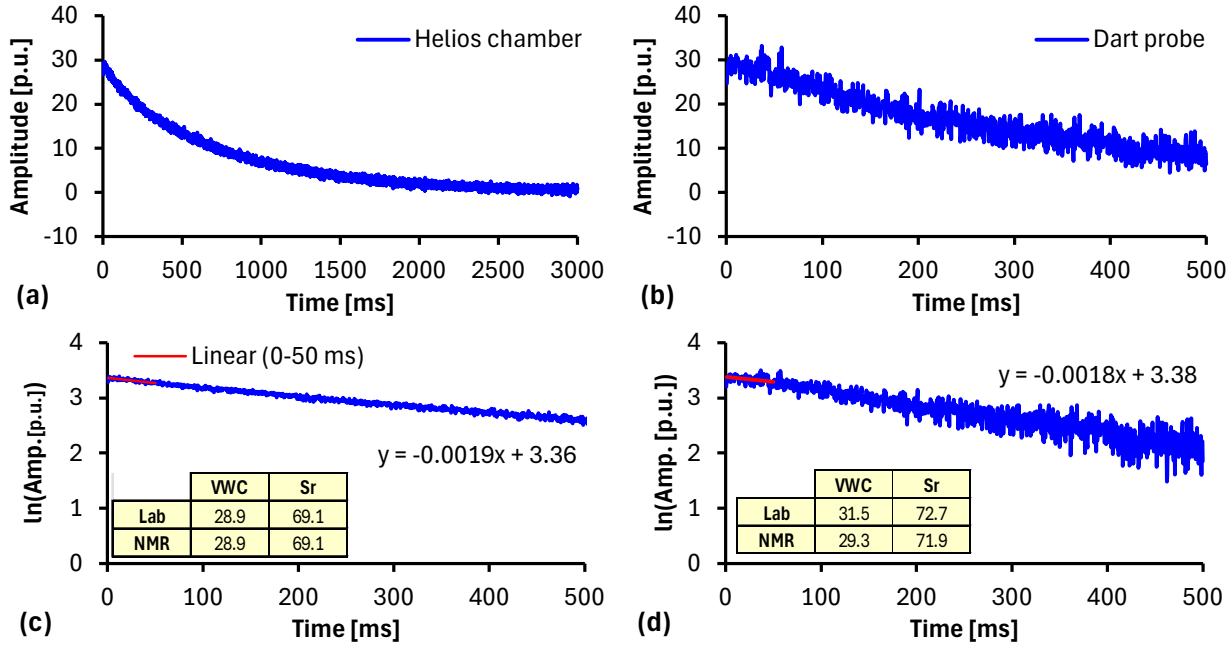

Figure 6. Illustration of the procedure to estimate VWC considering Ottawa sand (a) Helios multiexponential decaying curve, (b) Dart multiexponential curve, (c) logarithmic transformation and linear fitting (first 50 ms) to estimate VWC (Helios), (d) logarithmic transformation and linear fitting (first 50 ms) to estimate VWC (Dart).

Table 3. Summary of NMR measurements gathered with the Helios chamber

Material	te (ms)	Main sequence			Burst sequence		
		TR (s)	Scan length (ms)	Navg	TR (s)	Scan length (ms)	Navg
Tailings 1	0.2, 0.5, 1, 2	3 - 4	300	300	0.2	4	1800
Tailings 2	0.2, 0.5, 1, 2	3 - 4	300	300	0.2	4	1800
Tailings 3	0.2	3 - 4	300	300	0.2	4	1800
Tailings 4	0.2, 0.5, 1, 2	3 - 4	300	300	0.2	4	1800
Tailings 5	0.2, 0.5, 1, 2	3 - 4	300	300	0.2	4	1800
Tailings 6	0.2	3 - 4	300	300	0.2	4	1800
Tailings 7	0.2, 0.5, 1, 2	3 - 4	300	300	0.2	4	1800
Tailings 8	0.2, 0.5, 1, 2	3 - 4	300	300	0.2	4	1800
Ottawa Sand	0.5, 1, 2	3 - 13	3000	300	-	-	-

Table 4. Summary NMR measurements gathered with the Dart probe

Material	te (ms)	Main sequence			Burst sequence		
		TR (s)	Scan length (ms)	Navg	TR (s)	Scan length (ms)	Navg
Tailings 1	0.5	3	500	650	0.2	20	5200
Tailings 2	0.5	3	500	210	0.2	20	2100
Tailings 3	0.5	3	500	210	0.2	20	2100
Tailings 4	0.5	3	500	500	0.2	20	5000
Tailings 5	0.5	3	500	210	0.2	20	2100
Tailings 6	0.5	3	500	210	0.2	20	2100
Tailings 7	0.5	3	500	500	0.2	20	5000
Tailings 8	0.5	3	500	500	0.2	20	5000
Ottawa Sand	0.5	3	500	600	0.2	20	1200
Kaolinite	0.5	3	500	300	0.2	20	600

5.2 Signal-to-Noise Ratio (SNR)

Figure 7 shows the benefits of stacking (Navg is the number of stacks) on the signal-to-noise ratio SNR and ensuing the volumetric water VWC estimation. The reported SNR is computed as the ratio of the peak signal amplitude to the NMR signal's noise standard deviation. This procedure is consistent with conventional NMR processing (e.g., O'Haver, 1997). Results are presented for Tailings 4, with amplitudes in porosity units (p.u.), representing the percentage of water relative to a 100% water volume.

Figures 7a and 7b show that increasing the number of averages from Navg= 100 to 300 in the Helios and Navg= 50 to 500 in the Dart improves the signal-to-noise ratio from SNR= 40 to 60 and SNR= 10 to 30, respectively. The SNR increase is roughly proportional to the square root of the number of stacks, consistent with signal theory and statistical expectations (e.g., Santamarina & Fratta, 2005). The Helios chamber facilitates a higher SNR than the Dart probe. For instance, even after 500 stackings, the Dart's SNR remains lower than the Helios system at 100 stackings. The exponential decay curves also reflect this difference and the benefits of stacking. In the Helios, increasing Navg from 100 to 300 produces a minimal effect (Figure 7c), whereas in the Dart, noise decreases significantly between Navg=50 and Navg=500

(Figure 7d). This noise reduction comes at the expense of measurement time. For example, a Dart measurement with Navg=50 takes 7.5 minutes, whereas Navg=500 requires 1.25 hr.

Increasing SNR can also affect VWC estimates, as Figures 7e and 7f illustrate. This is because noise affects the determination of the exponential decay amplitude at $t = 0$. In the Helios (Figure 7e), the effect is minimal as SNR is already high at Navg=100. In contrast, Figure 7f shows that low stacking produces VWC errors up to 4% for the Dart, which decreases significantly as Navg increases to ~300. Thus, stacking is essential to increase SNR in NMR measurements conducted to infer the volumetric water content. Establishing target SNR is important to balance noise levels and time, particularly for field devices like the Dart, which require substantial stacking to increase SNR. The measurements reported here continued stacking until noise levels were acceptable or the measurement time was longer than 1.5 hours. Tables 3 and 4 provide the stacking information for the tested materials.

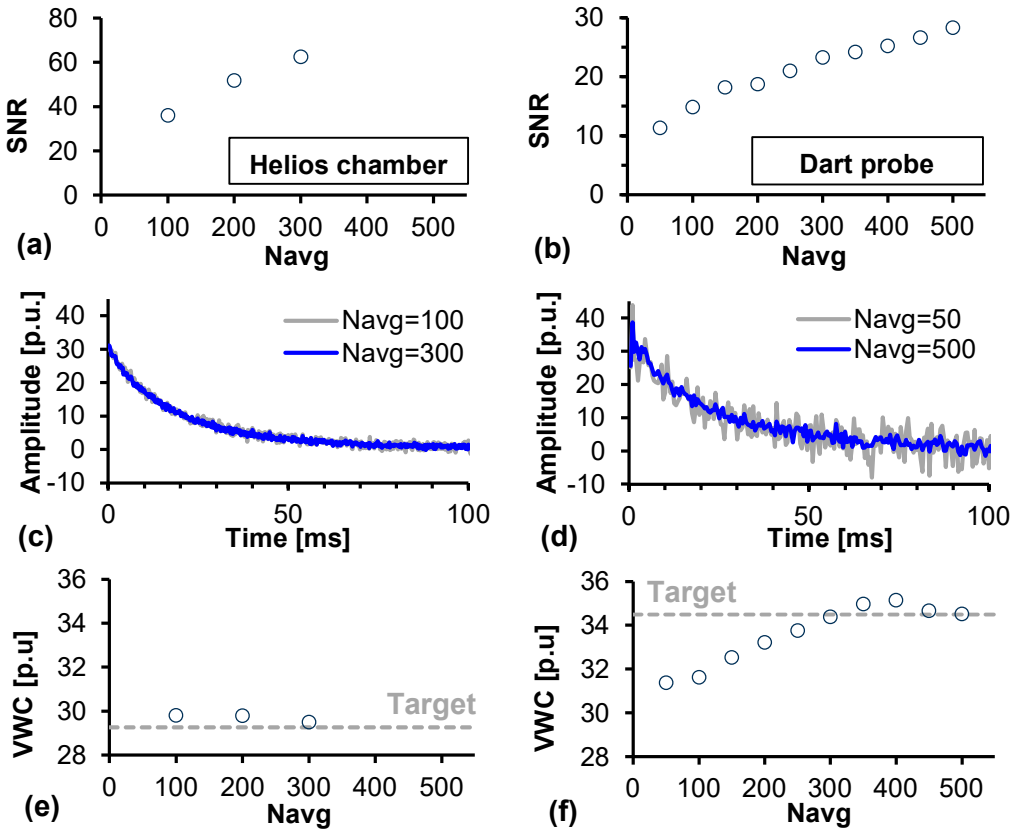

Figure 7. Influence of stacking (repeating measurements and averaging them Navg times) in SNR and NMR-based VWC estimates. (a, c, e) Helios chamber; (b, d, f) Dart probe (b, d, f).

5.3 Influence of gradation

NMR signals capture pore size information, making them sensitive to gradation (Figure 1e). Figure 8 illustrates this effect by comparing typical responses for the coarsest Tailings 4 and the finest Tailings 8 (characteristics in Figure 4 and Table 2), as well as for the two bounding soils, Ottawa sand and kaolinite. The exponential decay curves are normalized by their initial value at $t = 0$ to highlight their shape. Coarser materials are expected to exhibit a lower relaxation rate because the relaxation is inversely proportional to pore size. Figure 8a shows this effect by comparing measurements for Ottawa sand and Tailings 8 with the Helios chamber; by 20 ms, the Tailings 8 response has fully relaxed, whereas the Ottawa sand response continues to relax even after 500 ms. Similarly, measurements with the Dart probe show that the kaolinite's response fully decays by 150 ms, while Ottawa sand's relaxation extends beyond 500 ms (Figure 8c). Comparing Tailings 4 and 8 in the Helios chamber (Figure 8b) and Dart probe (Figure 8d) measurements shows similar effects, i.e., Tailings 8 (finer) relax faster. These observations are consistent with Peng & Keating (2021), who studied the effect of adding silt and clay to sand. In all mixtures, the decaying curves relaxed faster compared to pure sand. Notably, the tested tailings exhibit faster-decaying curves than the tested soils used as reference. In tailings, relaxation times remain below 100 ms, whereas relaxation times range from 200 ms (Kaolinite) to 3000 ms (Ottawa Sand). This faster relaxation likely results from the paramagnetic nature of most tested tailings, which is consistent with observations by Keating & Knight (2008) for paramagnetic sediments. Furthermore, fast decay requires higher resolution at short times to adequately assess the volumetric water content VWC; this is discussed next.

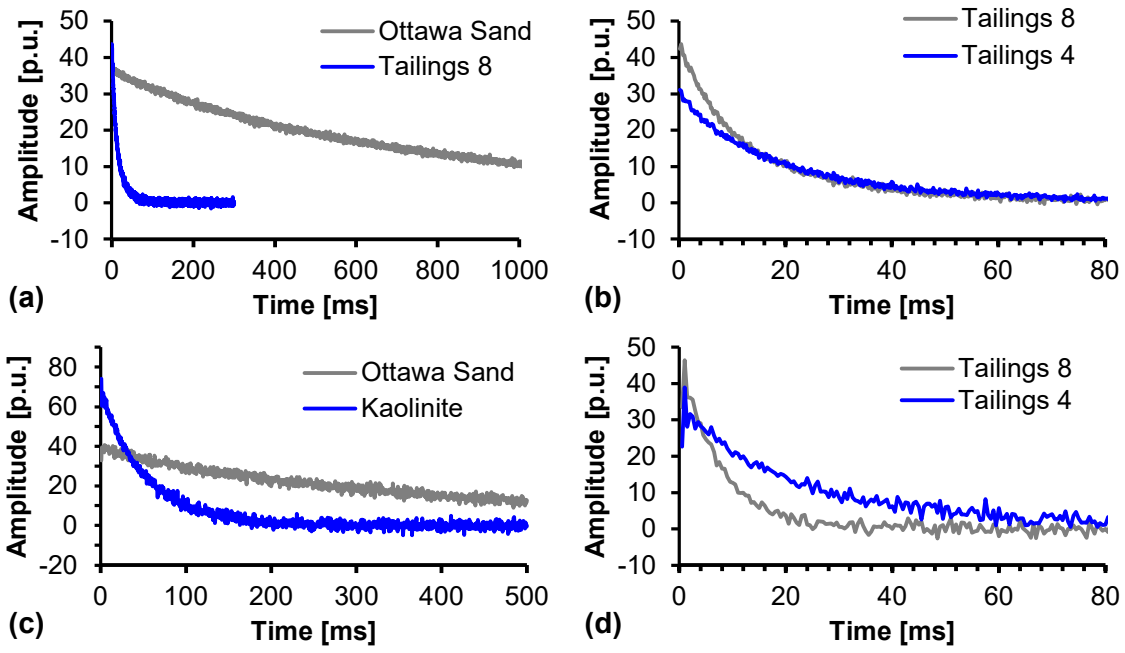

Figure 8. Illustration of exponential decaying curves in the coarser (Tailings 4) and finer (Tailings 8) tailings tested in this study, along with responses of the coarser (Ottawa sand) and finer (Kaolinite) tested materials. (a) Helios response for Tailings 8 and Ottawa sand, (b) Helios response of Tailings 4 and 8, (c) Dart response for Ottawa sand and kaolinite, and (d) Dart response for Tailings 8 and 4.

5.4 Influence of the echo time

Figure 9 illustrates how different echo times, t_e= 0.2, 0.5, 1.0, and 2.0 ms, affect VWC estimates in Tailings 4 (Figures 9a and 9b) and Tailings 5 (Figures 9c and 9d) using the Helios system. Both tailings have comparable magnetic susceptibility (Table 2), but Tailings 5 is finer (FC=52 %) than Tailings 4 (FC=29%), leading to faster exponential decay: the decay time in Tailings 5 is ~20 ms (Figure 9a), while it is ~50 ms in Tailings 4 (Figure 9c).

Increasing echo times t_e reduces the number of collected data points. For example, when t_e= 0.2 ms, the system collects 100 points between 0 and 20 ms, but only 10 points when t_e= 2.0 ms. Limited time resolution degrades the performance of all inversion methods for fast-decaying relaxations with short T_2 values. Figures 9b and 9d show how VWC estimates change as t_e increases. The shortest echo time t_e=0.2 ms yields the most accurate VWC estimates in both tailings. As t_e increases, the estimated VWC decreases, leading to a significant underestimation of ~22% in Tailings 5 when t_e=2 ms. The impact is more

pronounced in media with faster relaxation, such as Tailings 5 in Figure 9. The decreasing amplitude of the decay curves as the echo time increases points to diffusion relaxation caused by magnetic field gradients. In general, the measurements conducted as part of this study highlight the need for short echo times to properly resolve relaxations with short decay times. These observations align with Keating et al. (2020), who emphasized the benefits of short t_e values for VWC estimation in paramagnetic natural sediments.

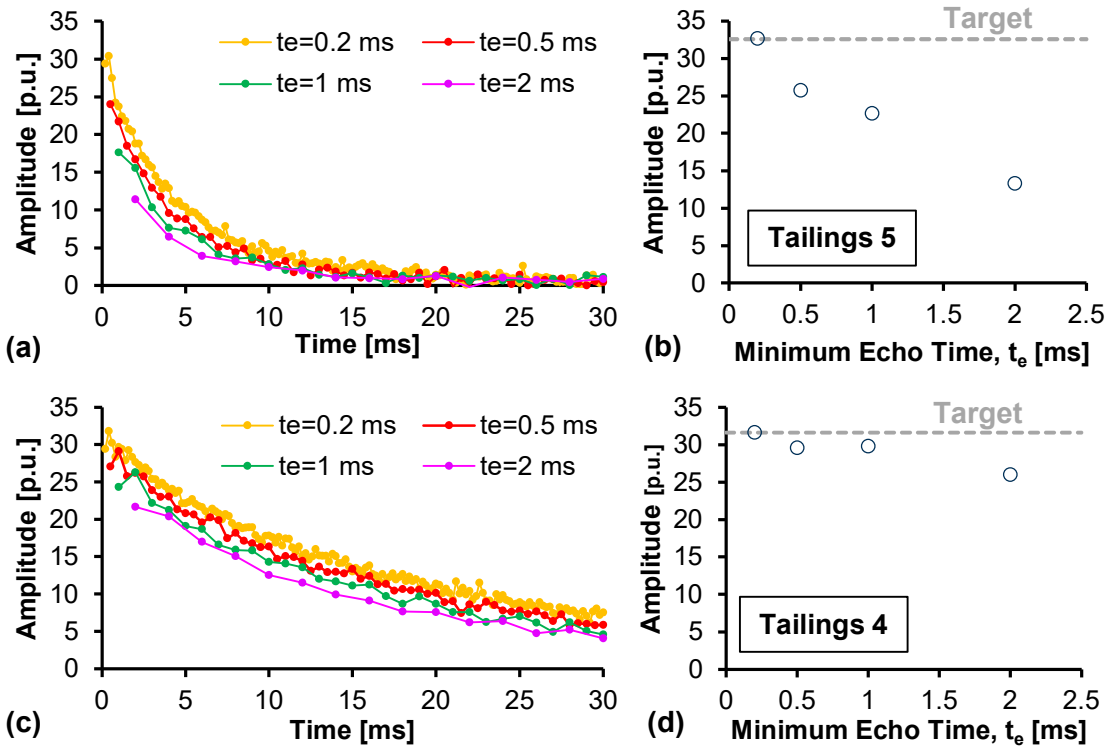

Figure 9. Influence of t_e in exponential decaying curves measured with the Helios system and NMR-based estimates of VWC. (a) Tailings 5 decaying curves for t_e=0.2, 0.5, 1.0, and 2.0 ms; (b) influence of t_e in Tailings 5 VWC estimates; (c) Tailings 4 decaying curves for t_e=0.2, 0.5, 1.0, and 2.0 ms; (b) influence of t_e in Tailings 4 VWC estimates.

5.5 Influence of magnetic susceptibility

Most tested tailings—Tailings 1, 2, 4, 5, 7, and 8—are paramagnetic, with χ values between 2.8 × 10^{-4} and 9.9 × 10^{-4} (classification in Dearing, 1994). In contrast, Tailings 3 and 6 are ferromagnetic with χ= 1.91 × 10^{-2} for Tailings 6 and χ=1.54 × 10^{-1} for Tailings 3. Figure 10 compares representative

measurements in paramagnetic tailings (Tailings 1) and ferromagnetic tailings (Tailings 3 and 6), considering both the Helios chamber and the Dart probe. Figures 10a and 10b show that Tailings 1 generates well-defined exponential decay curves in both systems, albeit with higher noise in Dart measurements consistent with previous discussions. The target VWC values, shown in the figure, closely match the y-axis intercept at time zero, indicating that NMR estimates align well with the target VWC.

The Helios system detects only noise for Tailings 6 and 3 (Figures 10c and 10e), as evident from the low y-axis intercepts (~ 0.4 %). On the other hand, Figure 10d shows some observable relaxation for Tailings 6 in the Dart probe, with better resolution at low times because the burst allowed for Navg=2100. Keating et al. (2020) anticipated this apparent improvement in systems with a magnetic field gradient, such as the Dart probe, as they help mitigate the effect of the internal magnetic gradients associated with paramagnetic minerals. However, this effect does not apply to the Helios system, which has an almost uniform magnetic field. Although the Dart appears to improve the decay curve shape, its NMR-based VWC estimates significantly underestimate the target values. For instance, in Figure 10d, the target VWC is 51.8%, but the Dart system estimates only 30.2%.

The apparent improvement is not observed in Tailings 3, with no measurable relaxation (Figure 10f). We attribute this to Tailings 3's exceptional high magnetic susceptibility. Magnetic mineral surfaces cause faster relaxation of H^+ protons, leading to faster decay of NMR signals (Foley et al., 1996; Jaeger et al., 2008; Keating & Knight, 2007). Additional internal magnetic fields around magnetic minerals are also induced, causing protons to relax at different frequencies, a phenomenon known as "line broadening" (Drain, 1962; Song, 2003). Furthermore, the random diffusion paths of water molecules (i.e., diffusion relaxation) prevent spin refocusing by the CPMG pulse sequence, leading to dephasing (Keating et al., 2020). The extent of dephasing depends on t_e: longer t_e results in greater dephasing, making shorter t_e values preferable to alleviate these effects, as experimentally observed in Figure 9.

5.6 Influence of tailings pond water

We obtained water from the ponds where the tailings 7 and 8 were deposited to assess the role of the collected water in NMR responses. The initial experiments involved containers filled with either tap water or pond water. Figure 11 presents the typical decay curves obtained using the Helios chamber (Figure 11a) and the Dart probe (Figure 11b) systems. Results show that the pond water exhibits a significantly faster relaxation than tap water. This faster relaxation aligns with the previously discussed relaxation effects of paramagnetic ions in solid minerals, except in this case, paramagnetic ions are dissolved in water (Jaeger et al., 2008).

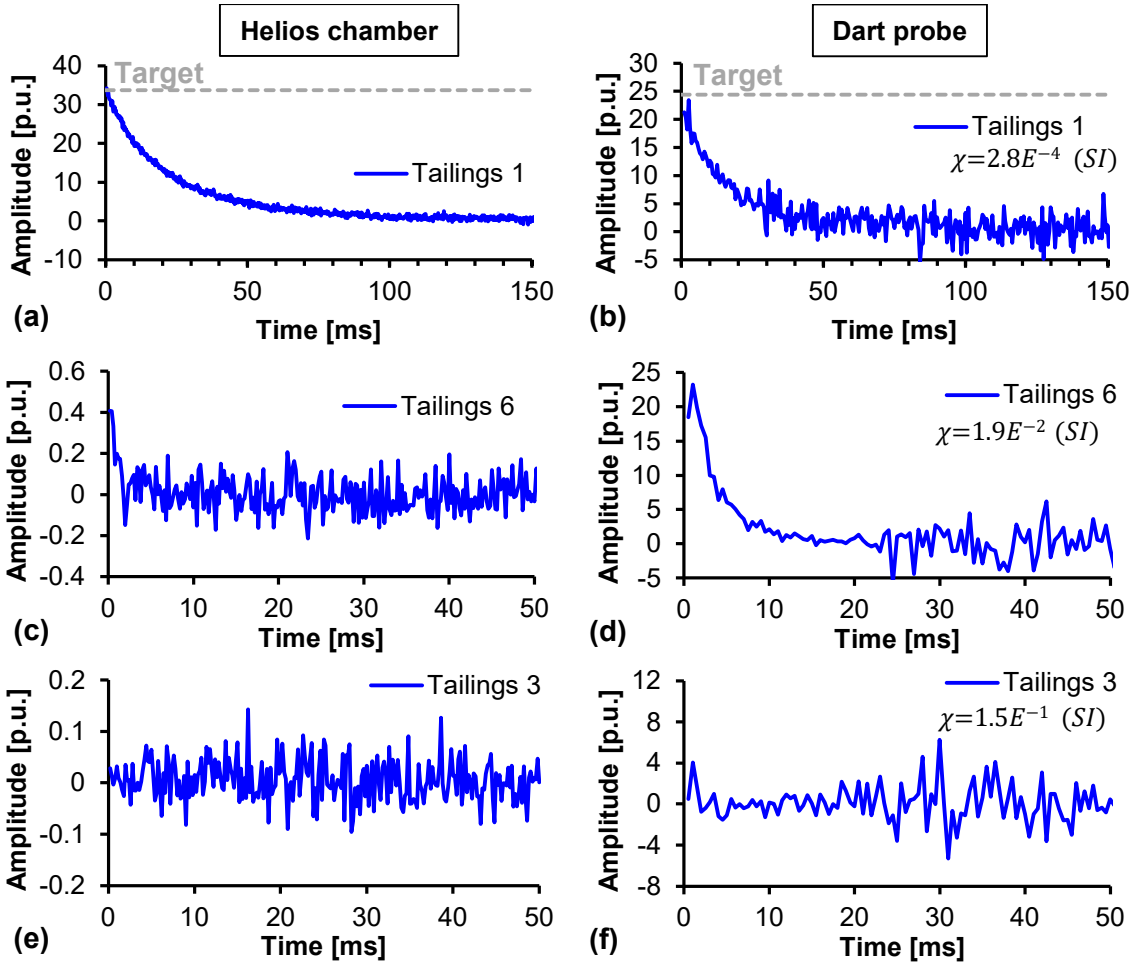

Figure 10. Influence of magnetic susceptibility in NMR measurements with the Helios (left column) and Dart (right column) systems. (a, b) typical decaying curves for Tailings 1 (χ=2.8 × 10^{-4}); (c,d) typical decaying curves for Tailings 6 (χ=1.91 × 10^{-2}); (e,f) typical decaying curves for Tailings 3 (χ=1.54 × 10^{-1})

355 This finding motivated us to evaluate the NMR response of tailings mixed with the two water
356 types. These experiments were conducted with the Helios system, following the previously described
357 procedures, except that the tap water was replaced by the pond water in the dry soil-fluid mix. Figures
358 12a and 12b compare normalized exponential decay curves for specimens with similar volumetric water
359 contents and high saturation but with different water fluids. Once again, relaxation occurs faster in
360 samples prepared with pond water, with the effect being more pronounced in the coarser tailings (Tailings
361 7). Furthermore, the water type effect differs in unsaturated samples. Figures 12c and 12d show
362 normalized exponential decay curves for Tailings 7 unsaturated specimens with saturations of 60% and
363 80%. For these unsaturated specimens the relaxation rates remain similar regardless of whether tap or
364 pond water is used, and the curves decay faster (~ 20 ms) compared to saturated samples (~40-60 ms),
365 which is consistent with faster relaxations observed in unsaturated samples (e.g., Falzone & Keating,
366 2016a). Despite the relaxation differences, the NMR performance on estimating VWC was similar for pond
367 or tap water. For instance, in Tailings 7 (Figure 12a), where target VWCs were 33.8% (tap water) and 33.0%
368 (pond water), the NMR estimates were 34.6% (tap water) and 32.0% (pond water). Similarly, in Tailings 8
369 (Figure 12b), where the target VWCs were 41.6% (tap water) and 40.9% (pond water), the NMR estimates
370 were 41.5% and 41.0%, respectively.

371 These results support the following conclusions: (1) Both water type and saturation influence
372 relaxation behavior, (2) the water chemistry has a marked effect on the T_2 spectrum as it affects relaxation
373 mechanisms. (3) The effect of water chemistry diminishes as pore size or saturation decreases because
374 surface relaxivity prevails. (4) The amplitude of the curve at time 0 is mostly controlled by the presence
375 of H+; therefore, NMR remains a good predictor of VWC regardless of water chemistry. This assumes there
376 are no other sources of H+ besides the original water, like alcohols, hydrocarbons, acids, amines, and
377 amides.

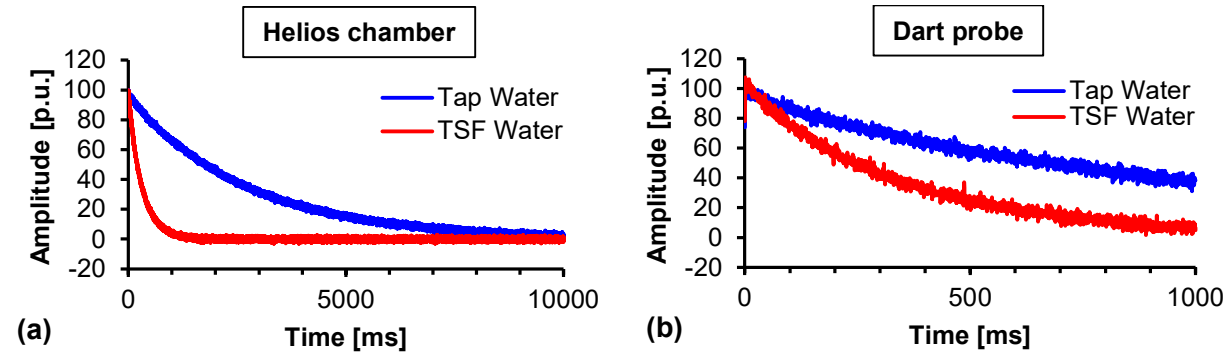

Figure 11. Influence of the fluid type (tap water versus tailings pond water) on NMR measurements (a) Tap vs. tailings pond water – Helios chamber, (b) Tap vs. tailings pond water – Dart probe

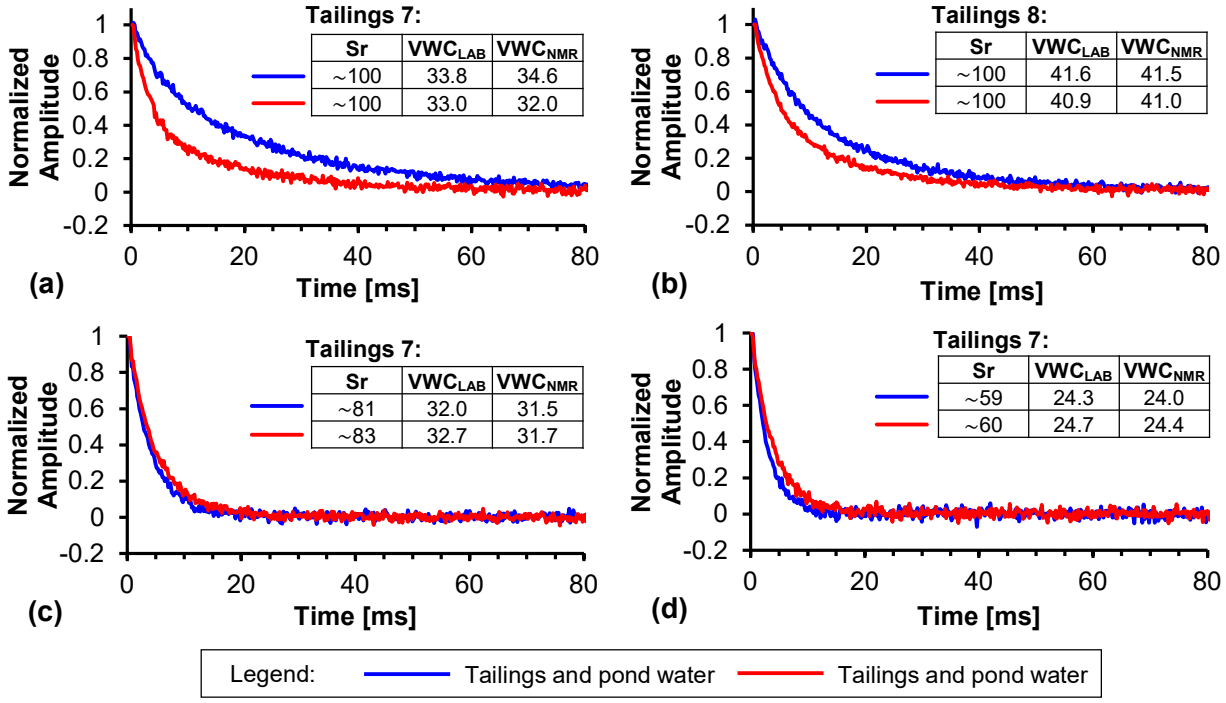

Figure 12. Influence of the fluid type (tap water versus tailings pond water) on NMR measurements with the Helios in saturated and unsaturated samples (a) Tailings 7 responses – Sr ~100%, (b) Tailings 8 responses – Sr ~100%, (c) Tailings 7 responses – Sr ~80%, and (d) Tailings 7 responses - Sr ~60%.

6 Performance Estimating Volumetric Water Content and Saturation.

Figure **Error! Reference source not found.** compares target volumetric water content values VWC_{LAB} with NMR-based estimates VWC_{NMR} using the Helios chamber. The NMR estimates closely match the target values, with an average difference of 0.44% when the magnetic susceptibility is $\chi<10^{-3}$ and t_e =0.2, except for Tailings 2, which has a particular behavior to be discussed later. The data collected for the

ferromagnetic Tailings 3 and 6 is dominated by noise, preventing any extraction of VWC information from the NMR signal. In general, lower echo times t_e values (e.g., 0.2 ms) improve accuracy. For instance, increasing t_e to 0.5 ms increases the average prediction error to 2.8%, particularly when finer tailings are involved (Tailings 5, 7, and 8), in agreement with earlier discussions (Section 5.5).

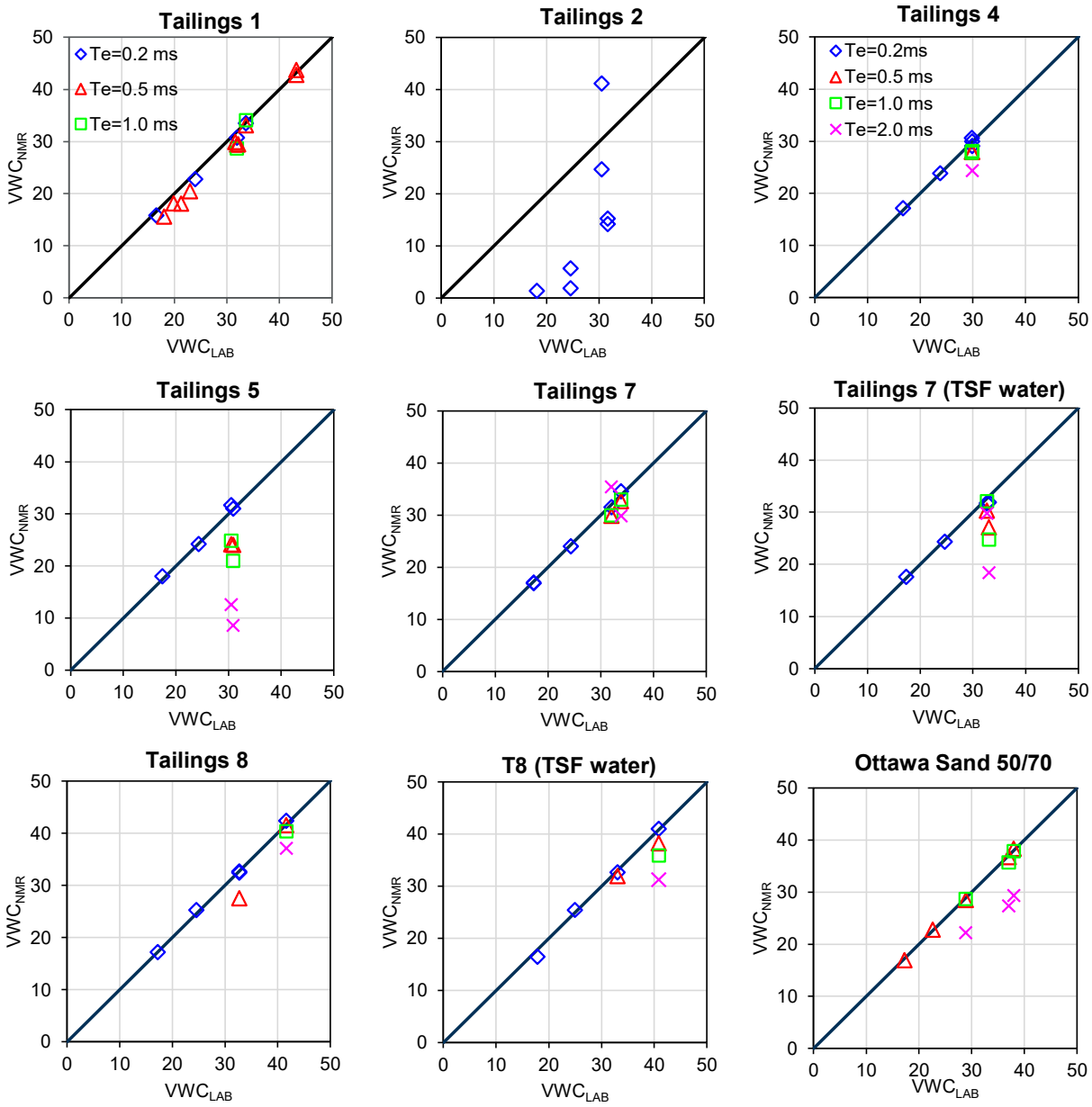

Figure 13. Comparison between VWC_{LAB} and VWC_{NMR} on testing with the NMR Helios chamber.

For Dart measurements, most tailings with χ<10^{-3} show similar trends (except for Tailings 5 and 2), with an average difference of 1.7% between target values and NMR estimates (Figure **Error! Reference source not found.**). The trend for Tailings 5 is as expected (i.e., NMR estimates increase as target values increase); however, there is a higher discrepancy with target water contents than Helios-based measurements, averaging 0.4% in Helios and 1.7% in Dart (see Figures **Error! Reference source not found.** and 14). This discrepancy likely results from the Dart's minimum echo time $t_e = 0.5$ ms, the faster relaxation due to the more plastic fines of Tailings 5 (fast relaxation ~35 ms), and the Dart probe's lower SNR. The Helios system captures these curves with better resolution and higher SNR than the Dart (see Sections 5.1 and 5.3). Additionally, specimen preparation is more complex for the Dart tests, particularly when more plastic fines are involved.

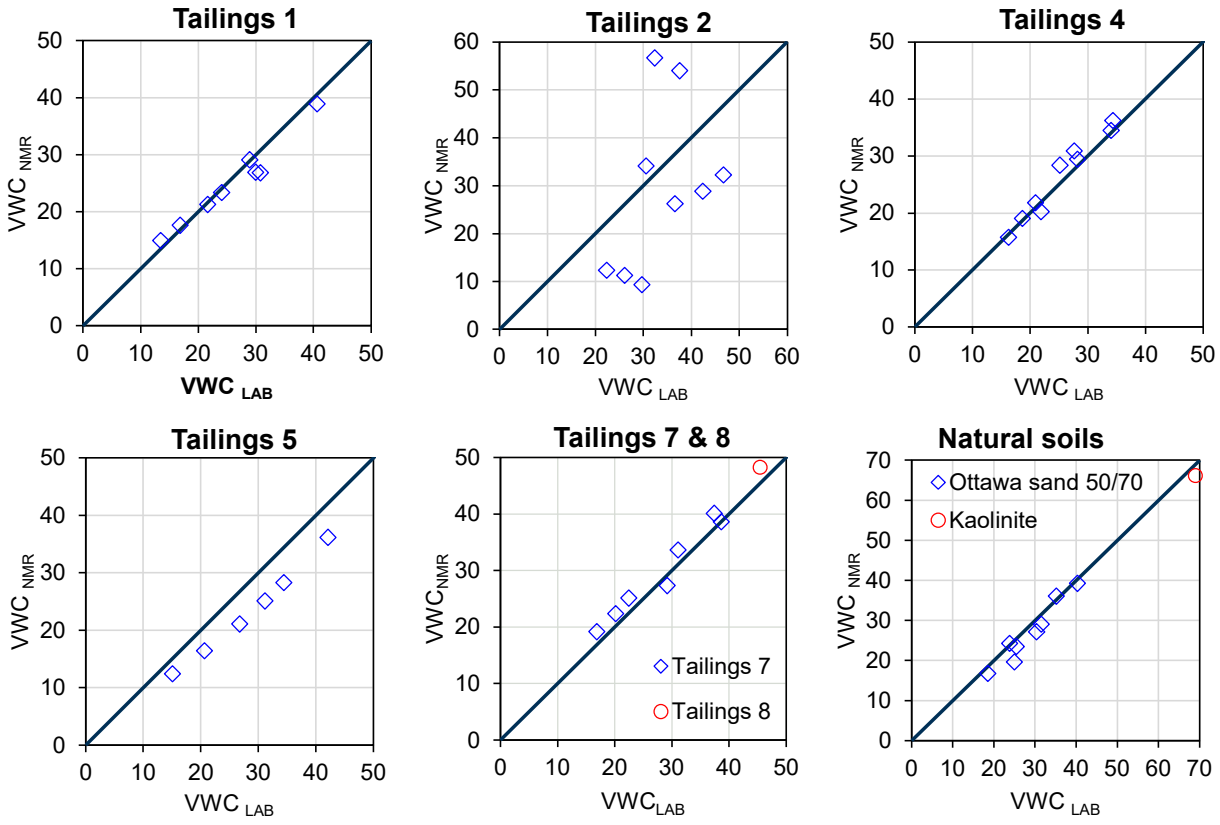

Figure 14. Comparison between VWC_{LAB} and VWC_{NMR} on testing with the NMR Dart probe.

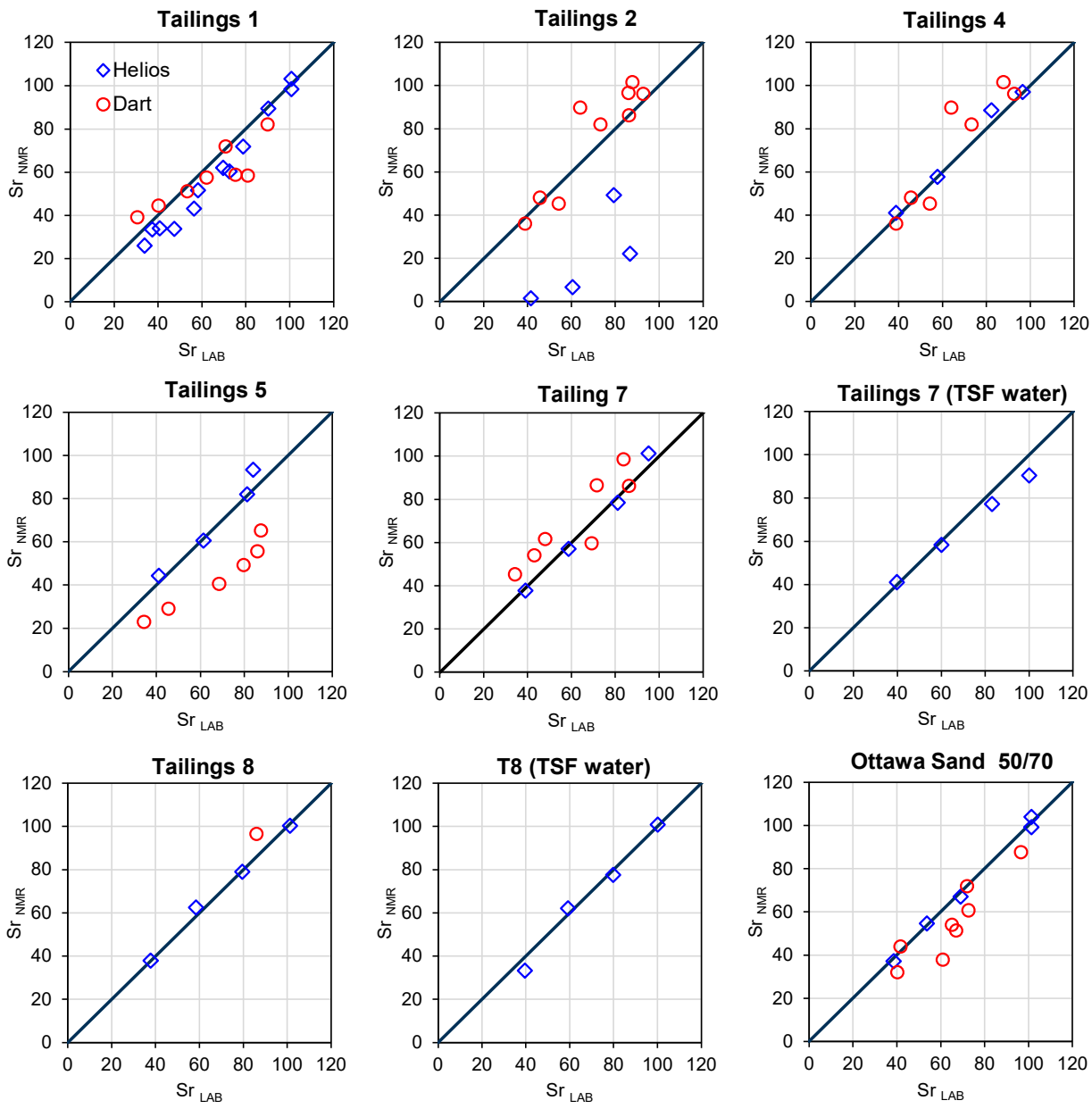

Figure 15. Comparison between SrLab and Sr_{NMR}. Sr_{NMR} is estimated from NMR testing (Helios and Dart) using Equation 2 – refer to the text for additional details.

Figure 15 compares target and NMR-based saturation estimates using both Helios and Dart measurements. The target saturation is calculated using volumetric/gravimetric relationships, while the NMR-based estimate follows Equation 2, where VWC comes from NMR measurements, and GWC is controlled during the experiments (Helios results include t_e=0.2 ms only). NMR-based saturation estimates follow target values trend. As target saturation increases, NMR estimates also increase, with

most data aligning close to the 1:1 lines. The average saturation difference between target and NMR estimates for the Helios is 3% (excluding Tailings 2). For the Dart, the average difference is 10% (excluding Tailings 2 and 5, which show higher discrepancies). These differences stem from errors in the NMR-based VWC estimates and also depend on the saturation level, as discussed next.

7 Discussion

7.1 Influence of NMR-based volumetric water content errors in saturation estimates

The error in the prediction of saturation dSr due to an error in the measured volumetric water content $dVWC$ can be predicted from the partial derivative $d(Sr)/d(VWC)$ of Equation 2 (e.g., Bevington & Robinson (1969); see details in Appendix B).

$$dSr = \left(\frac{Sr}{GWC}\right)^2 dVWC \tag{3}$$

Where gravimetric water content GWC is directly measured as in our laboratory tests, or determined from recovered samples following standard practice in field applications. Figure 16 illustrates the application of Equations 2 and 3, showing how dSr varies with saturation and gravimetric water content GWC for errors $dVWC$=0.5, 1.0, 2.0, 3.0, and 4.0%. The GWC values 20% and 30% are selected as representative of coarse and fine tailings at saturation levels above 85% (Macedo & Vergaray, 2022). Figure 16 enables key observations: (1) Considering that fine tailings generally have higher GWC than coarse tailings, the estimation of saturation is less sensitive to error in VWC for fine tailings. For example at $dVWC$=0.5% and Sr=90%, dSr is 4% when GWC=20% and 1.5% when GWC=30%; (2) at a given saturation, errors in saturation scale linearly with errors in volumetric water content. For instance, when GWC=30% and Sr=90%, dSr changes from about 2% to 16% as $dVWC$ increases from 0.5% to 4%; (3) the effect of saturation on dSr is complex; for a given $dVWC$ dSr increases at a faster rate as saturation increases. However, a saturation increase can also increase GWC, causing counteracting effects (see Equation 2 and Figure 16).

For the average errors observed in this study, $dVWC$ =0.4% for Helios and $dVWC$ =1.7% for Dart, Figure 16 provides estimates of dSr at Sr values near 90%. The estimated error in saturation is dSr= 1.5 to 3% with the Helios-based $dVWC$ and dSr= 7 to 10% with the Dart-based. The Dart system can be deployed in the field, making the associated errors particularly relevant for subsurface investigations estimating saturation. Reducing the estimated errors further would require improvements in field NMR devices to implement shorter echo times and a higher signal-to-noise ratio SNR. There are efforts in this direction. For example, we are aware of recent variations of the Dart device used in this study, including enhanced sensor electronics that increase SNR by a factor of 2.0. Increasing stacking in targeted layers can also help reduce errors by improving SNR.

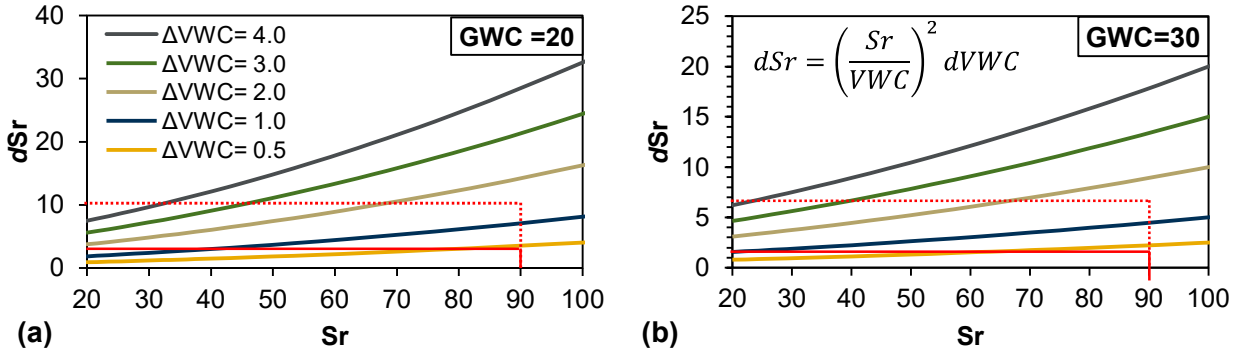

Figure 16. dSr variation in terms of $dVWC$, Sr, and GWC (a) GWC=20%, (b) GWC=30%. Gs is 2.7; the continuous lines correspond to dSr estimates based on average VWC errors with the Helios system, the dotted lines show the same information for the VWC Dart-based error.

7.2 Influence of magnetic susceptibility and iron form

NMR performed poorly in estimating VWC for ferromagnetic tailings with $\chi > 1.9 \times 10^{-2}$, specifically Tailings 3 and 6. These tailings contain high Fe concentrations (7.3% in Tailings 6 and 48.9% in Tailings 3 (see Table 2). In contrast, NMR-based VWC estimates matched well target values for most paramagnetic tailings with $\chi < 10^{-3}$, except for Tailings 2, even though its magnetic susceptibility is low (χ= 3.4×10^{-4}). This suggests that magnetic susceptibility alone is insufficient to predict the expected performance of NMR measurements.

458 Tailings 2 contains 4.1% Fe by mass, a concentration comparable to that of Tailings 1 (4.2%).
459 However, X-ray diffraction analysis reveals a key difference: Tailings 2 contains Sanidine and Hydronium
460 Jarosite, where iron is in ferric Fe^{3+} state, while Tailings 1 contain Pyrite and Ankerite, where iron is in
461 ferrous Fe^{2+} state. Jaeger et al. (2008) demonstrated that proton relaxation accelerates in the presence of
462 Fe^{3+} relative to Fe^{2+}. Similarly, Keating and Knight (2007) highlighted that both the presence and
463 mineralogical form of Fe influence NMR relaxation. Therefore, the poor NMR performance in Tailings 2 is
464 likely due to Fe^{3+}, which increases surface relaxivity. For comparison, Tailings 4, 7, and 8 contain only Fe^{2+},
465 while Tailings 5 contains both Fe^{2+} and Fe^{3+}, but at a significantly lower Fe concentration (0.4%) than
466 Tailings 2.

467 **8 Conclusions**

468 This study evaluates the potential of NMR for estimating volumetric water content and saturation
469 in mine tailings. We characterized eight mine tailings by measuring magnetic susceptibility χ, iron content,
470 and mineralogy to infer Fe-state. These tailings were then analyzed using two benchtop NMR systems
471 with different signal-to-noise ratios and magnetic fields. A linear fitting procedure proposed in this study
472 was applied to estimate water content and saturation from NMR, and the results were compared against
473 controlled volumetric and gravimetric measurements.

474 The findings highlight the key role of magnetic susceptibility, mineralogy, and strongly
475 paramagnetic elements (e.g., Fe^{3+}) in NMR performance. NMR performed well for most paramagnetic
476 tailings with $\chi < 1.0 \times 10^{-3}$ but performed poorly for ferromagnetic tailings with $\chi > 1.9 \times 10^{-2}$. However,
477 magnetic susceptibility alone is not sufficient to predict performance. For instance, NMR underestimated
478 water content due to the presence of iron in ferric Fe^{3+} state, such as Fe-bearing sanidine and hydronium
479 jarosite, which results in fast NMR relaxation.

480 NMR differentiated the response of coarse and fine tailings, with fine tailings exhibiting faster
481 decay curves (<20 ms). These results, consistent with previous studies on natural soils, highlight the

advantages of using short echo times and maintaining a high signal-to-noise ratio SNR. Short echo times help mitigate the effects of diffusion-induced relaxation in fast-decaying signals, while a high SNR reduces measurement error. Tailings pond water primarily affected the NMR decay curves in highly saturated tailings, though it had minimal impact on water content estimates, particularly when short echo time data are available.

The results show significant potential of NMR for applications in tailings engineering; NMR performed well in estimating water content in five of the eight tailings. However, caution is necessary. Before large-scale field investigations, we recommend assessing the material's magnetic susceptibility, mineralogy, and Fe content. Conducting benchtop NMR tests, such as those conducted with the Helios system, can help anticipate NMR behavior before field deployment.

The uncertainty in saturation estimates is directly influenced by errors in NMR-based water content estimates and the saturation level. NMR accuracy in estimating water content depends on signal quality, emphasizing the need for improvements in signal-to-noise ratio and field NMR resolution. Ongoing efforts in these areas are promising. Future work should also focus on reducing echo time in field devices, as tailings exhibit rapid signal decay. For saturation characterization, a multi-method approach is recommended. NMR fast-logging, CPTu, P-wave measurements, and continuum borehole GWC can provide broad saturation patterns and identify key layers before conducting high-stacking NMR measurements. While time-intensive, this approach can enhance saturation estimate accuracy.

9 Data Availability Statement

Some or all data, models, or code that support the findings of this study are available from the corresponding author upon reasonable request.

10 Acknowledgments

This study was funded by the Tailings and Industrial Waste Engineering (TAILENG) Foundation, with additional support from ConeTec. We gratefully acknowledge ConeTec for providing in-kind access

506 to the NMR devices used in this study. We also thank Vista Clara Inc. for valuable discussions on the
507 interpretation of NMR data and for generously hosting a Georgia Tech graduate student at their
508 Washington office for a one-week technical exchange.

509

510

References

Alves Filho, E. G., Alexandre e Silva, L. M., & Ferreira, A. G. (2015). Advancements in wastewater characterization through NMR spectroscopy. *Magnetic Resonance in Chemistry*, *53*(9), 648–657.

Anaraki, M. T., Lysak, D. H., Downey, K., Kock, F. V. C., You, X., Majumdar, R. D., Barison, A., Lião, L. M., Ferreira, A. G., & Decker, V. (2021). NMR spectroscopy of wastewater: A review, case study, and future potential. *Progress in Nuclear Magnetic Resonance Spectroscopy*, *126*, 121–180.

Behroozmand, A. A., Keating, K., & Auken, E. (2015). A review of the principles and applications of the NMR technique for near-surface characterization. *Surveys in Geophysics*, *36*, 27–85.

Behroozmand, A. A., Knight, R., Müller-Petke, M., Auken, E., Barfod, A. A. S., Ferré, T. P. A., Vilhelmsen, T. N., Johnson, C. D., & Christiansen, A. V. (2017). Successful sampling strategy advances laboratory studies of NMR logging in unconsolidated aquifers. *Geophysical Research Letters*, *44*(21), 11–21.

Bevington, P. R., & Robinson, D. K. (1969). *Data reduction and error analysis for the physical sciences* (1st Edition, Vol. 336). McGraw-Hill.

Bloch, F. (1946). Nuclear induction. *Physical Review*, *70*(7–8), 460.

Carr, H. Y., & Purcell, E. M. (1954). Effects of diffusion on free precession in nuclear magnetic resonance experiments. *Physical Review*, *94*(3), 630.

Chen, S., & Li, L. (2019). Wireline, LWD, and surface NMR instruments and applications for petroleum reservoir formation evaluation. *Journal of Machining and Forming Technologies*, *11*(3/4), 131–187.

Coates, G. R., Xiao, L., & Prammer, M. G. (1999). NMR logging. *Principles and Interpretation. Halliburton Energy Service, Huston, Texas*.

534 Conte, P., Chillura Martino, D. F., & Lo Meo, P. (2024). *The Meaning of Pollution and the Powerfulness*
535 *of NMR Techniques*.
536 Costabel, S., & Yaramanci, U. (2011). Relative hydraulic conductivity and effective saturation from
537 Earth's field nuclear magnetic resonance–a method for assessing the vadose zone. *Near*
538 *Surface Geophysics*, *9*(2), 155–167.
539 Dearing, J. A. (1994). *Environmental magnetic susceptibility: using the Bartington MS2 system*. Chi
540 Pub.
541 Dlubac, K., Knight, R., Song, Y., Bachman, N., Grau, B., Cannia, J., & Williams, J. (2013). Use of NMR
542 logging to obtain estimates of hydraulic conductivity in the High Plains aquifer, Nebraska, USA.
543 *Water Resources Research*, *49*(4), 1871–1886.
544 Drain, L. E. (1962). The broadening of magnetic resonance lines due to field inhomogeneities in
545 powdered samples. *Proceedings of the Physical Society*, *80*(6), 1380.
546 Dunn, K.-J., Bergman, D. J., & LaTorraca, G. A. (2002). *Nuclear magnetic resonance: Petrophysical and*
547 *logging applications*. Elsevier.
548 Falzone, S., & Keating, K. (2016a). A laboratory study to determine the effect of pore size, surface
549 relaxivity, and saturation on NMR T2 relaxation measurements. *Near Surface Geophysics*, *14*(1),
550 57–69.
551 Falzone, S., & Keating, K. (2016b). The NMR relaxation response of unconsolidated sediments during
552 drainage and imbibition. *Vadose Zone Journal*, *15*(6).
553 Fassel, V. A., & Kniseley, R. N. (1974). Inductively coupled plasma. Optical emission spectroscopy.
554 *Analytical Chemistry*, *46*(13), 1110A – 1120a.
555 Foley, I., Farooqui, S. A., & Kleinberg, R. L. (1996). Effect of paramagnetic ions on NMR relaxation of
556 fluids at solid surfaces. *Journal of Magnetic Resonance, Series A*, *123*(1), 95–104.

557 Fu, T.-F., Xu, T., Heap, M. J., Meredith, P. G., Yang, T., Mitchell, T. M., & Nara, Y. (2021). Analysis of
558 capillary water imbibition in sandstone via a combination of nuclear magnetic resonance
559 imaging and numerical DEM modeling. *Engineering Geology*, *285*, 106070.
560 Jaeger, F., Bowe, S., Van As, H., & Schaumann, G. E. (2009). Evaluation of 1H NMR relaxometry for
561 the assessment of pore-size distribution in soil samples. *European Journal of Soil Science*, *60*(6),
562 1052–1064.
563 Jaeger, F., Rudolph, N., Lang, F., & Schaumann, G. E. (2008). Effects of soil solution's constituents on
564 proton NMR relaxometry of soil samples. *Soil Science Society of America Journal*, *72*(6), 1694–
565 1707.
566 Keating, K., & Falzone, S. (2013). Relating nuclear magnetic resonance relaxation time distributions
567 to void-size distributions for unconsolidated sand packs. *Geophysics*, *78*(6), D461–D472.
568 Keating, K., & Knight, R. (2007). A laboratory study to determine the effect of iron oxides on proton
569 NMR measurements. *Geophysics*, *72*(1), E27–E32.
570 Keating, K., & Knight, R. (2008). A laboratory study of the effect of magnetite on NMR relaxation
571 rates. *Journal of Applied Geophysics*, *66*(3–4), 188–196.
572 Keating, K., Walsh, D. O., & Grunewald, E. (2020). The effect of magnetic susceptibility and magnetic
573 field strength on porosity estimates determined from low-field nuclear magnetic resonance.
574 *Journal of Applied Geophysics*, *179*, 104096.
575 Kendrick, A. K., Knight, R., Johnson, C. D., Liu, G., Knobbe, S., Hunt, R. J., & Butler Jr, J. J. (2021).
576 Assessment of NMR logging for estimating hydraulic conductivity in glacial aquifers.
577 *Groundwater*, *59*(1), 31–48.
578 Kirkland, C. M., & Codd, S. L. (2018). Low-field borehole NMR applications in the near-surface
579 environment. *Vadose Zone Journal*, *17*(1), 1–11.

580 Kirkland, C. M., Zanetti, S., Grunewald, E., Walsh, D. O., Codd, S. L., & Phillips, A. J. (2017). Detecting
581 microbially induced calcite precipitation in a model well-bore using downhole low-field NMR.
582 *Environmental Science & Technology*, *51*(3), 1537–1543.
583 Knight, R., Walsh, D. O., Butler Jr, J. J., Grunewald, E., Liu, G., Parsekian, A. D., Reboulet, E. C., Knobbe,
584 S., & Barrows, M. (2016). NMR logging to estimate hydraulic conductivity in unconsolidated
585 aquifers. *Groundwater*, *54*(1), 104–114.
586 Levitt, M. H. (2008). *Spin dynamics: basics of nuclear magnetic resonance*. John Wiley & Sons.
587 Ling, N. N. A., Hussaini, S. R., Elsayed, M., Connolly, P. R. J., El-Husseiny, A., Mahmoud, M., May, E.
588 F., & Johns, M. L. (2022). Model synthetic samples for validation of NMR signal simulations.
589 *Transport in Porous Media*, *142*(3), 623–639.
590 Macedo, J., & Vergaray, L. (2022). Properties of mine tailings for static liquefaction assessment.
591 *Canadian Geotechnical Journal*, *59*(5), 667–687.
592 Meiboom, S., & Gill, D. (1958). Modified spin-echo method for measuring nuclear relaxation times.
593 *Review of Scientific Instruments*, *29*(8), 688–691.
594 Motta, C., Bryan, J., & Kantzas, A. (2008). Characterization of Oil Sands Tailings using Nuclear
595 Magnetic Resonance (NMR) Technique. *10th International Mine Water Association Congress*.
596 Motta Cabrera, S. C., Bryan, J. L., & Kantzas, A. (2010). Estimation of bitumen and solids content in
597 fine tailings using low-field NMR technique. *Journal of Canadian Petroleum Technology*, *49*(07),
598 8–19.
599 Nasharuddin, R. (2023). *Probing Cemented Paste Backfill using Nuclear Magnetic Resonance*
600 *Relaxometry and Uniaxial Compressive Strength to Understand Rapid Hydration Rate for*
601 *Mining Operations*.

Novotny, E. H., deAzevedo, E. R., de Godoy, G., Consalter, D. M., & Cooper, M. (2023). Determination of soil pore size distribution and water retention curve by internal magnetic field modulation at low field 1H NMR. *Geoderma*, *431*, 116363.

O'Haver, T. (1997). A pragmatic introduction to signal processing. *University of Maryland at College Park*.

Pehme, P., Crow, H., Parker, B., & Russell, H. (2022). Evaluation of slim-hole NMR logging for hydrogeologic insights into dolostone and sandstone aquifers. *Journal of Hydrology*, *610*, 127809.

Peng, Y., & Keating, K. (2021). A laboratory study of the effect of clay, silt, and sand content on low-field nuclear magnetic resonance relaxation time distributions. *Geophysics*, *86*(5), WB1–WB8.

Perlo, J., Danieli, E., Perlo, J., Blümich, B., & Casanova, F. (2013). Optimized slim-line logging NMR tool to measure soil moisture in situ. *Journal of Magnetic Resonance*, *233*, 74–79.

Purcell, E. M., Torrey, H. C., & Pound, R. V. (1946). Resonance absorption by nuclear magnetic moments in a solid. *Physical Review*, *69*(1–2), 37.

Reid, D., Fourie, A., Fridjonsson, E., Jervis-Bardy, N., Reyes, M., & Nuriakhmetov, R. (2023). Potential Application of Nuclear Magnetic Resonance to Infer In Situ Degree of Saturation in Tailings. *Journal of Geotechnical and Geoenvironmental Engineering*, *149*(5), 02823003.

Santamarina, J. C., & Fratta, D. (2005). *Discrete signals and inverse problems: an introduction for engineers and scientists*. John Wiley & Sons.

Santamarina, J. C., Klein, K. A., Wang, Y. H., & Prencke, E. (2002). Specific surface: determination and relevance. *Canadian Geotechnical Journal*, *39*(1), 233–241.

Song, Y. (2003). Using internal magnetic fields to obtain pore size distributions of porous media. *Concepts in Magnetic Resonance Part A: An Educational Journal*, *18*(2), 97–110.

Spurlin, M. S., Barker, B. W., Cross, B. D., & Divine, C. E. (2019). Nuclear magnetic resonance logging: Example applications of an emerging tool for environmental investigations. *Remediation Journal*, *29*(2), 63–73.

Sucre, O., Pohlmeier, A., Minière, A., & Blümich, B. (2011). Low-field NMR logging sensor for measuring hydraulic parameters of model soils. *Journal of Hydrology*, *406*(1–2), 30–38.

Walsh, D., Grunewald, E., Turner, P., Hinnell, A., & Ferre, T. P. A. (2014). Surface NMR instrumentation and methods for detecting and characterizing water in the vadose zone. *Near Surface Geophysics*, *12*(2), 271–284.

Walsh, D., Turner, P., Grunewald, E., Zhang, H., Butler Jr, J. J., Reboulet, E., Knobbe, S., Christy, T., Lane Jr, J. W., & Johnson, C. D. (2013). A small-diameter NMR logging tool for groundwater investigations. *Groundwater*, *51*(6), 914–926.

Zhao, B., & Santamarina, J. C. (2022). Fine-grained sediment characterization and process monitoring using nuclear magnetic resonance (NMR). *Geotechnical Testing Journal*, *45*(4), 877–890.